

Combining Electromagnetic and Gravitational-Wave Constraints on Neutron-Star Masses and Radii: Supplemental Material

Mohammad Al-Mamun¹, Andrew W. Steiner^{1,2}, Joonas Nättilä^{3,4}, Jacob Lange⁵, Richard O’Shaughnessy⁵, Ingo Tews⁶, Stefano Gandolfi⁶, Craig Heinke⁷, and Sophia Han^{8,9}

¹*Department of Physics and Astronomy, University of Tennessee, Knoxville, TN 37996, USA*

²*Physics Division, Oak Ridge National Laboratory, Oak Ridge, TN 37831, USA*

³*Physics Department and Columbia Astrophysics Laboratory,*

Columbia University, 538 West 120th Street, New York, NY 10027, USA

⁴*Center for Computational Astrophysics, Flatiron Institute, 162 Fifth Avenue, New York, NY 10010, USA*

⁵*Rochester Institute of Technology, 85 Lomb Memorial Drive, Rochester, NY 14623, USA*

⁶*Theoretical Division, Los Alamos National Laboratory, Los Alamos, NM 87545, USA*

⁷*Department of Physics, CCIS 4-183, University of Alberta, Edmonton, AB, T6G 2E1, Canada*

⁸*Department of Physics, University of California, Berkeley, CA 94720, USA and*

⁹*Department of Physics and Astronomy, Ohio University, Athens, OH 45701, USA*

METHOD

Probability distributions from NS observations

As in Refs. [1, 2], we include mass and radius constraints from seven quiescent low mass X-ray binaries (QLMXBs) in the globular clusters 47 Tuc (the QLMXB X7), ω Cen, NGC 6397, NGC 6304, M 13, M 28, and M 30. We include distance uncertainties, and the possibility for either H or He atmospheres as in Ref. [1], but we assume that the temperature is uniform and do not consider the possible effects of hotspots (we do not assume a uniform temperature distribution for the NICER source J0030+0451 below).

We include mass-radius constraints from PRE X-ray bursters SAX J1810.8–429 and 4U 1724–307 performed using the cooling-tail method [3]. We also include mass and radius constraints from Ref. [4] on the PRE X-ray burster 4U 1702–429, obtained using the direct atmosphere model fit method. We focus only on their model “D” results: this corresponds to a parameter optimization with the most relaxed initial prior assumptions where the hydrogen fraction is treated as a free parameter. We have selected three bursting low-mass X-ray binary systems that have PRE X-ray bursts detected in the “hard” accretion disk state, where the disk is thought to truncate far away from the star and the $M - R$ measurements produce valid solutions that are not biased towards the $R = 4GM/c^2$ line [5].

Refs. [6, 7] obtained mass and radius constraints using an analysis of NICER X-ray timing data on PSR J0030+0451. We used the results from Ref. [6], but expect that results using the constraints from Ref. [7] would be similar.

The X-ray observations may not include all of the systematics. Our analysis combines mass and radius constraints which were obtained from different methods, and this combination mitigates some of these systematics. A method to quantify additional unknown systematics is to

fold an additional intrinsic uncertainty in both the mass and the radius for each measurement. In our case, this would require an additional 22 parameters (or 24 parameters with the NICER data). We find that this larger parameter space increases the computational cost significantly. To moderate this cost, we define a single Intrinsic Scattering (IS) parameter, σ , for each neutron star. We fix the width of the Gaussian in the mass direction to be $\sigma_M \equiv (1.4 M_\odot)\sigma$ and the width in the radius direction to be $\sigma_R \equiv (5 \text{ km})\sigma$. Thus, there is only one coupled intrinsic scattering parameter for each neutron star for which we have EM data. Using this, the two-dimensional probability distribution for the mass and radius, $\mathcal{D}(\mathcal{R}, \mathcal{M})$ is modified to

$$\mathcal{D}_{\text{IS}}(R, M, \sigma) = \frac{1}{\mathcal{N}} \int_{R_0}^{R_1} \int_{M_0}^{M_1} dR' dM' \mathcal{D}(R', M') \times \exp \left[-\frac{1}{2} \left(\frac{R - R'}{\sigma_R} \right)^2 - \frac{1}{2} \left(\frac{M - M'}{\sigma_M} \right)^2 \right], \quad (1)$$

where $\mathcal{N} = \int_V D_{\text{IS}} dV$ is a normalization factor preserving the probability density over the total volume V . We note that in theory \mathcal{N} is just a normalization related to an integral over a multivariate Gaussian, but in practice the finite boundary effects complicate it therefore it is easiest to evaluate the integral numerically. We limit $\log_{10}\sigma$ to be between -2 and 2 . We show below that modifying the upper limit would not change our result. When $\sigma = 0.01$, the result from Eq. 1 is essentially identical to the original version thus lowering our lower limit would only bias our posteriors towards small values of σ .

There are several alternatives for the procedure which we chose. One could express the uncertainty in terms of the compactness M/R or the GR-corrected radius $R_\infty = R(1 - 2GM/Rc^2)^{-1/2}$ instead of M and R . Also, one could choose a different smoothing kernel than a Gaussian function. Different choices of the kernel or the variables on which the Gaussian is written would particularly impact the tails of the posterior distributions.

An examination of alternatives, however, will be left to future work.

For the data from GW170817 [8], we interpolate a marginal likelihood for binary parameters $\mathcal{M}_{\text{det}}, \delta m, \tilde{\Lambda}, \chi_{1,z}, \chi_{2,z}$, integrating over nuisance extrinsic parameters like source orientation relative to the line of sight. Provided by RIFT [9], this marginal likelihood is a function of the dimensionless NS spins $\chi_{i,z}$ relative to the orbital angular momentum direction $\hat{L} = \hat{z}$, the binary chirp mass in the detector frame

$$\mathcal{M}_{\text{det}} = \frac{(M_1 M_2)^{3/5}}{(M_1 + M_2)^{1/5}} (1 + z) \quad (2)$$

where z is the redshift of the merger, the mass difference $\delta m \equiv M_1 - M_2$, and the combined tidal deformability

$$\tilde{\Lambda} = \frac{16}{13} \frac{(M_1 + 12M_2) M_1^4 \Lambda_1 + (M_2 + 12M_1) M_2^4 \Lambda_2}{(M_1 + M_2)^5}. \quad (3)$$

Empirically, the marginal likelihood for GW170817 does not appreciably depend on the antisymmetric combination $\Delta\tilde{\Lambda}$. We then further marginalize this five-dimensional over the two dimensionless spins to produce a three-dimensional marginal likelihood which depends only on $\mathcal{M}_{\text{det}}, \delta m, \tilde{\Lambda}$.

As discussed in Refs. [10, 11], we require an additional nuisance parameter for each neutron star, which we choose to be the mass: M_1 and M_2 , for the neutron stars involved in GW170817, and M_3, M_4, \dots for the neutron stars which have photon-based mass and radius constraints. In addition, the QLMXBs have an additional parameter η_i which chooses between a H or He atmosphere for each particular object i . Presuming our EOS model has parameters $\{p\}$, the conditional probability is just the product

$$\begin{aligned} \mathcal{P}(D|M) = & D_{\text{LIGO}}[\mathcal{M}_{\text{det}}(M_1, M_2, z), \delta m(M_1, M_2), \\ & \tilde{\Lambda}(M_1, M_2, \{p\})] \\ & \times \prod_{i=3}^{N+3} D_i[R(M_i, \{p\}), M_i, \eta_i, \sigma_i] \end{aligned} \quad (4)$$

where P_{QMC} is described below and N is 11 when the NICER data is included and 10 otherwise.

All prior probability distributions are flat between boundaries which do not impact the final results, except for (i) the parameters a, α, b , and β (described below) which follow a multivariate Gaussian distribution, (ii) the intrinsic scattering parameters which are flat in $\log_{10} \sigma_i$ between -2 and 2 , and (iii) the redshift of GW170817 which is a Gaussian distribution with peak at 0.0099 and width of 0.0009 [8]. Our full prior probability also contains several choices about our model construction which are described below.

EOS Model

We describe nuclear matter near saturation with an approach very similar to that from Ref. [12]. For this, we need to model both pure neutron matter (PNM) and symmetric nuclear matter (SNM). Pure neutron matter (i.e., vanishing proton fraction) can be well-described with a parameterization proposed in Ref. [13];

$$E_{\text{PNM}}(n_{\text{B}}) = a \left(\frac{n_{\text{B}}}{n_0} \right)^{\alpha} + b \left(\frac{n_{\text{B}}}{n_0} \right)^{\beta}. \quad (5)$$

In order to recast the parameters in terms of the symmetry energy S and its derivative L , we use the relations

$$\begin{aligned} S &= a + b + 16 \text{ MeV} \\ L &= 3(a\alpha + b\beta). \end{aligned} \quad (6)$$

We selected parameter sets for a, α, b , and β based on the neutron-matter calculations of Ref. [14], where local chiral EFT interactions of Refs. [15, 16] were combined with the auxiliary field diffusion Monte Carlo method [17] to obtain the energy per particle of neutron matter with theoretical uncertainty estimates. The parameters a, b, α and β are selected from uniform priors in the intervals $[0, 20]$, $[0, 20]$, $[0, 1]$ and $[1, 10]$, respectively. For each parameter set, we check if the resulting curve for $E_{\text{PNM}}(n_{\text{B}})$ falls within the uncertainty band of Ref. [14] in the density range from $(0.5 - 1.0) n_0$. In addition, we check if the resulting pressure at saturation density falls within the predicted range. For all $\mathcal{O}(1000)$ parameter sets that pass these tests, we fit the probability distribution to a four-dimensional Gaussian, and then select those four parameters according to that Gaussian distribution. For symmetric nuclear matter (i.e., equal neutron and proton fractions) we select a random Skyrme model from a list of 1000 models provided by the authors of Ref. [18] (see also Ref. [19]). Our final nuclear-matter EOS is then given by

$$\begin{aligned} E(n_{\text{B}}, x) = & E_{\text{Skyrme}}(n_{\text{B}}, x = 0.5) + [(1 - 2x)^2 E_{\text{PNM}}(n_{\text{B}}) \\ & - E_{\text{Skyrme}}(n_{\text{B}}, x = 0.5)]. \end{aligned} \quad (7)$$

To construct neutron-star matter, we determine the proton fraction in beta-equilibrium by ensuring that $\mu_n = \mu_p + \mu_e$.

For higher densities, we use two different EOS parameterizations. The first is an EOS based on three polytropic segments, each given by $P = K\epsilon^{\Gamma}$, where the adiabatic index $\Gamma \equiv 1 + 1/n$ and n is the polytropic index. This model is similar to Model A of Refs. [1, 20] and also similar to that from Ref. [21] as used by the LIGO and VIRGO collaborations in Ref. [8]. The QMC results are used up to the energy density which corresponds to twice the nuclear saturation density. Beyond that energy density, the first polytrope, with index n_1 , is used. The second polytrope, with index n_2 , begins at energy density

Label	EOS parameterizations and data selection
(a)	3P with GW only
(b)	4L with GW only
(c)	3P with {GW, QLMXB, PRE}
(d)	4L with {GW, QLMXB, PRE}
(e)	3P with {GW, QLMXB, PRE, NICER}
(f)	4L with {GW, QLMXB, PRE, NICER}
(g)	3P with {GW, QLMXB, PRE, NICER} w/int. scat.
(h)	4L with {GW, QLMXB, PRE, NICER} w/int. scat.

TABLE I. Legend explaining EOS parameterizations and data sets used in the figures. The three-polytrope model is labeled “3P”, and the four line-segment model is labeled “4L”.

ε_1 , and ends at energy density ε_2 . The third polytrope, with index n_3 , is used for all higher energy densities. We use uniform prior distributions for these five EOS parameters. The coefficients K are fixed to ensure the EOS is continuous. This model is labeled “3P” below.

There may be a phase transition in high-density matter, but strong phase transitions imply extreme values of Γ and K in polytropic models and, thus, are disfavored by our choice of uniform prior distributions. Therefore, we choose an alternative EOS parametrization which more naturally includes phase transitions. In this parametrization, the EOS is constructed by a set of line segments which change slope at fixed energy densities, 400, 600, and 1000 MeV/fm³. The first line segment begins at the energy density which corresponds to twice the nuclear saturation density and has pressure P_1 at 400 MeV/fm³. The next three line segments have pressures P_2 , P_3 , and P_4 at energy densities of 600, 1000, and 1400 MeV/fm³, respectively. We choose uniform prior distributions for these four pressure parameters. This model is labeled “4L” below. All polytropes (if one extrapolates them to lower densities) go through the origin at $P = \epsilon = 0$, thus they must be finally tuned to have a pressure which decreases weakly with density. On the other hand, line segments need not go through the origin and thus more easily represent a strong phase transition.

Finally, the dimensionless speed of sound squared, $c_s^2/c^2 = dP/d\epsilon$ is constrained to be between 0 and 1 at all densities below the central pressure of the maximum-mass neutron star.

Neutron-star structure

We presume the neutron stars are spherical, non-rotating, objects with $T = 0$. The Tolman-Oppenheimer-Volkov (TOV) equations [22, 23] are solved to compute the neutron-star mass and radius as a function of the central pressure. We ensure the maximum mass is at least two solar masses in our baseline calculation in order to match recent observations of high-mass

neutron stars [24–26]. Ref. [26] implies a larger mass, $2.14^{+0.10}_{-0.09} M_\odot$, but also a larger uncertainty. We can always refine the selection of posterior samples to increase the maximum mass if necessary. We compute the moment of inertia as a function of the gravitational mass using the Hartle approximation [27]. Ref. [28] showed the existence of a strong correlation between the scaled moment of inertia ($\bar{I} \equiv I/M^3$) and the scaled tidal Love deformability ($\bar{\Lambda} \equiv \lambda/M^5$). We use the relation provided in Ref. [29] to calculate the dimensionless tidal deformabilities of the NSs;

$$\ln \bar{\Lambda} \simeq -30.5395 + 38.3931 (\ln \bar{I}) - 16.307 (\ln \bar{I})^2 + 3.36972 (\ln \bar{I})^3 - 0.26105 (\ln \bar{I})^4 \quad (8)$$

See also Ref. [30] for an updated analysis on the relationship between \bar{I} and $\bar{\Lambda}$.

Computational details

We use the affine-invariant sampling method proposed by Ref. [31] which simulates the object function with an ensemble of “walkers”. This sampling method decreases autocorrelation lengths, especially when the underlying distribution does not have complicated geometrical features or multimodalities. We use four times as many walkers as parameters. The cost of the affine-invariant method, which becomes more significant for larger parameter spaces, is that the time for the ensemble of walkers to equilibrate can be long. In our simulation, equilibration of an ensemble of walkers can require several days of computing time. However, once the ensemble is equilibrated, the autocorrelation length is small in comparison (half a day of computing time). One can create an equilibrated ensemble on only one thread, and then copy that equilibrated ensemble to many threads before simulating in parallel. We also spread out our walkers for one ensemble over many OpenMP threads, but to avoid complexities associated with multiple threads accessing or modifying the same walker at the same time, walkers are only updated after all walkers in the ensemble have undergone a “stretch move” (in the parlance of Ref. [31]). This slightly increases the autocorrelation length, but the OpenMP parallelization benefit far outweighs this cost. The MPI parallelization is trivial, except for coordination to ensure that many MPI ranks do not read or write from disk at the same time.

The folding of the data with the Gaussian in Eq. (1) can be handled with the use of FFTs. However, doing this directly for each neutron star at each Monte Carlo point is time-consuming. Thus, we cache the result of the FFT over a wide range of values for the intrinsic scattering parameter, generating a data cube covering R , M and σ for each source. We use linear interpolation in this data cube at each point to compute the conditional

Model & data	-2σ	-1σ	$+1\sigma$	$+2\sigma$
(a) 3P, GW	11.30	11.59	13.33	13.95
(b) 4L, GW	10.65	11.25	12.36	13.09
(c) 3P, GW, QLMXB, PRE	11.21	11.69	12.29	12.55
(d) 4L, GW, QLMXB, PRE	11.27	11.65	12.10	12.31
(e) 3P, all	11.28	11.72	12.30	12.58
(f) 4L, all	11.32	11.67	12.12	12.34
(g) 3P, all+IS	11.18	11.6	12.39	12.75
(h) 4L, all+IS	11.12	11.54	12.14	12.45

TABLE II. The 1σ and 2σ credible intervals for the radius of a $1.4 M_{\odot}$ NS in km. Rows 7 and 8 include all the electromagnetic (EM) constraints (QLMXB, PRE, & NICER), convolved with intrinsic scattering (IS).

probability described above. The 8 simulations required about 500k core-hours of computational time.

FURTHER RESULTS

Table II summarizes the constraints on the radius of a $1.4 M_{\odot}$ NS, based on Fig. 1 in the main paper.

Tidal deformabilities in GW170817

The posteriors for the tidal deformabilities for the two stars in the GW170817 merger are given in Fig. 1. Panels (g) and (h) are slightly different, corresponding to slightly different EOS information, and this is comparable with the variation shown in Fig. 10 in Ref. [8]. Adding the X-ray data shrinks the posteriors significantly, and now the posteriors for the tidal deformabilities are less sensitive to the addition of the data set or the EOS choice, as seen in panels (a), (b), (c) and (d).

Intrinsic Scattering Parameters

The posterior distributions for the intrinsic scattering parameters provide insight into which objects are most likely to contain systematic uncertainties (Fig. 2). The small radius implied when an H atmosphere is fit to the neutron star in NGC 6397 gives it a larger probability of a larger value of σ . Previous work on QLMXBs [1] also found that this object was more difficult to fit. The QLMXB and NICER objects generally have larger intrinsic scattering parameters than the PRE objects, but this may originate from the small size of our data set.

Posterior distributions for the neutron star masses for our results which include the IS parameters are given in Fig. 3. The top two panels show the normalized posterior distributions for all of the neutron stars. The LIGO

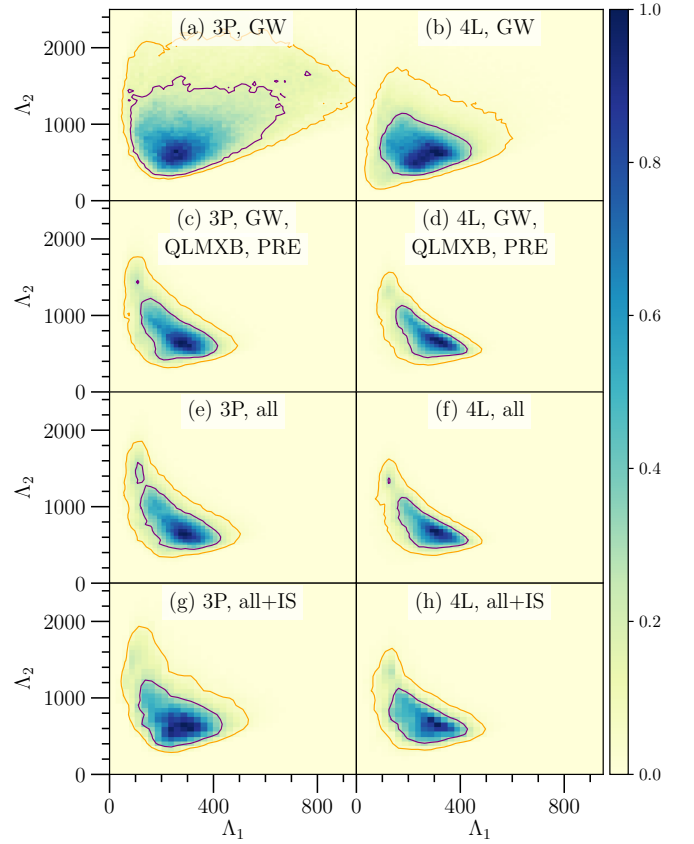


FIG. 1. Joint posterior distribution for Λ_2 and Λ_1 density plot with contour lines which enclose 68% or 95% of the probability distribution. Left panels are constructed with the “3P” EOS and right panels with the “4L” EOS. Different rows refer to different data selections. In each panel, the density plot is renormalized so that the peak is at 1.

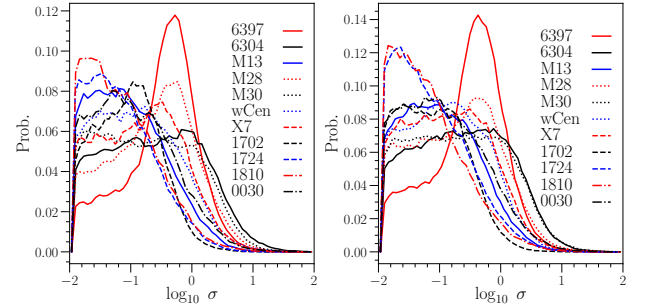


FIG. 2. The normalized posterior distributions for the intrinsic scattering parameters.

posteriors are more strongly-peaked because the GW observations more accurately determine the neutron star masses. The bottom two panels show the mass posteriors grouped by the kind of observation: from QLMXBs, from NSs which have PRE X-ray bursts, from the star observed by NICER, and from the LIGO NSs. We find that the PRE X-ray burst sources tend to have slightly larger masses and the NICER source is more likely to

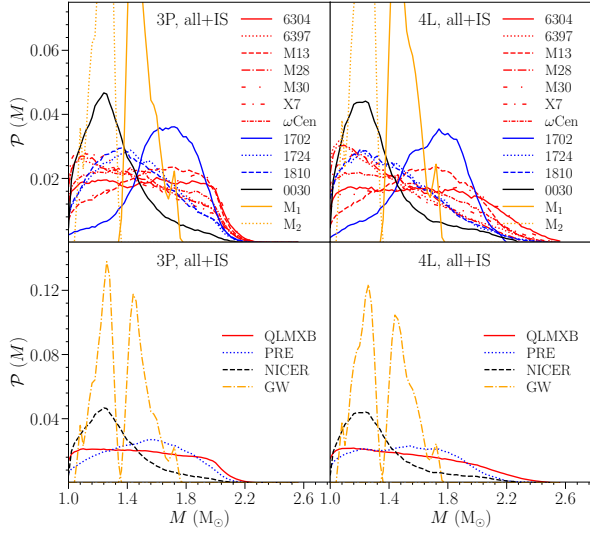


FIG. 3. The normalized posterior distributions of NS masses from intrinsic scattering models, 3P in the left column and 4L in the right. The top two panels show posteriors for individual NSs while the bottom two panels provide posteriors for different groups of NSs.

$M (M_\odot)$	$R (km)$			
	-2σ	-1σ	$+1\sigma$	$+2\sigma$
1.00	11.20	11.63	12.42	12.76
1.10	11.19	11.62	12.41	12.77
1.20	11.19	11.61	12.41	12.77
1.30	11.19	11.61	12.40	12.77
1.40	11.18	11.60	12.39	12.75
1.50	11.17	11.59	12.37	12.73
1.60	11.13	11.56	12.35	12.68
1.70	11.09	11.53	12.34	12.65
1.80	11.00	11.45	12.30	12.60
1.90	10.88	11.36	12.26	12.56
2.00	10.59	11.14	12.17	12.51
2.10	10.77	11.25	12.16	12.51
2.20	11.04	11.43	12.20	12.52
2.30	11.23	11.57	12.23	12.51
2.40	11.53	11.77	12.29	12.52

TABLE III. The 68% and 95% credible intervals for neutron star radii (in km) using the 3P EOS model, the GW data, and the EM data including IS, referred to as “3P, all+IS”.

have a smaller mass. The mass posteriors extend well above $2.2 M_\odot$, especially for the 4L parameterization, indicating that the true maximum mass may be this large. Tables III and IV give the 68% and 95% credible intervals for neutron star radii for a range of masses. The corresponding credible intervals for the pressure for a range of energy densities are given in Table V and VI.

$M (M_\odot)$	$R (km)$			
	-2σ	-1σ	$+1\sigma$	$+2\sigma$
1.00	10.88	11.16	11.86	12.38
1.10	10.95	11.27	11.92	12.37
1.20	11.01	11.36	11.98	12.38
1.30	11.07	11.46	12.06	12.40
1.40	11.12	11.54	12.14	12.45
1.50	11.15	11.58	12.19	12.49
1.60	11.16	11.61	12.24	12.53
1.70	11.15	11.67	12.30	12.58
1.80	11.11	11.70	12.36	12.62
1.90	11.04	11.70	12.39	12.64
2.00	10.85	11.68	12.44	12.66
2.10	10.87	11.70	12.47	12.67
2.20	11.05	11.75	12.50	12.69
2.30	11.21	11.80	12.52	12.70
2.40	11.37	11.85	12.55	12.77
2.50	11.53	11.89	12.56	12.71
2.60	11.74	11.99	12.52	12.73
2.70	11.98	12.13	12.47	12.62

TABLE IV. The 68% and 95% credible intervals for neutron star radii (in km) using the 4L EOS model, the GW data, and the EM data including IS, referred to as “4L, all+IS”.

Tidal Deformability Correlations

There are correlations and/or universal relations which have been used to analyze observations which constrain neutron star structure. We can test the validity of these assumptions in the context of our EOS parameterizations.

Ref. [32] showed that there is a correlation between the symmetric tidal parameter ($\Lambda_s = \Lambda_2 + \Lambda_1$) and the antisymmetric part ($\Lambda_a = \Lambda_2 - \Lambda_1$)

$$\Lambda_{a,YY} = F_n^{(\Lambda_a)}(q) \Lambda_s^{-\alpha} \frac{a + \sum_{i=1}^3 \sum_{j=1}^2 b_{ij} q^j \Lambda_s^{-i/5}}{a + \sum_{i=1}^3 \sum_{j=1}^2 c_{ij} q^j \Lambda_s^{-i/5}} \quad (9)$$

where

$$F_n^{(\Lambda_a)}(q) \equiv \frac{1 - q^{10/(3-n)}}{1 + q^{10/(3-n)}}, \quad (10)$$

and the values of the parameters a , α , b_{ij} , c_{ij} , and n , are given in Ref. [32]. We compare $\Lambda_{a,YY}$ with the exact value Λ_a in Fig. 4. We find that $\Lambda_{a,YY}$ is generally an overestimate, with deviations as large as 30%. This effect may come from the fact that they use an EOS library that has many EOSs with smaller radii, and our observational constraints restrict us from sampling this part of the parameter space. Presuming this correlation is exact will tend to underestimate Λ_a . These deviations are different in the two EOS models, and in the 4L model they tend to be larger for smaller values of Λ_a .

ϵ (MeV/fm ³)	P (MeV/fm ³)			
	-2σ	-1σ	$+1\sigma$	$+2\sigma$
200	3.53	4.03	5.18	5.84
300	9.98	12.57	18.75	22.52
400	30.52	36.76	51.18	60.91
500	60.39	66.24	99.96	119.7
600	99.08	115.5	157.0	172.2
700	144.8	162.3	204.5	226.1
800	186.2	203.2	253.8	281.9
900	217.1	244.1	308.7	340.6
1000	251.2	288.1	374.0	413.3
1100	280.2	322.6	427.4	476.6
1200	309.1	356.1	480.5	542.1
1300	338.3	390.0	535.1	613.8
1400	367.7	423.8	591.4	688.6
1500	405.1	464.6	661.2	786.7
1600	437.9	500.5	720.1	859.7

TABLE V. The 68% and 95% credible intervals for the pressure (in MeV/fm⁻³) using the 3P EOS model, the GW data, and the EM data including IS, referred to as “3P, all+IS”.

ϵ (MeV/fm ³)	P (MeV/fm ³)			
	-2σ	-1σ	$+1\sigma$	$+2\sigma$
200	3.14	3.28	4.42	5.17
300	5.82	8.09	14.96	18.68
400	28.98	44.31	73.61	78.55
500	69.40	96.60	144.3	164.2
600	100.3	150.5	229.2	253.5
700	152.7	174.2	262.7	313.8
800	180.7	207.0	326.5	398.1
900	195.2	249.7	430.3	505.4
1000	214.3	294.2	515.8	588.1
1100	250.5	343.2	566.4	652.9
1200	276.7	391.5	631.8	733.2
1300	300.1	433.3	706.6	821.0
1400	330.5	476.8	789.0	904.2
1500	369.4	550.4	891.5	949.3
1600	382.6	591.5	929.3	957.6

TABLE VI. The 68% and 95% credible intervals for the pressure (in MeV/fm⁻³) using the 3P EOS model, the GW data, and the EM data including IS, referred to as “3P, all+IS”.

Ref. [33] found that the ratio of the dimensionless tidal deformabilities, $\Lambda_{\text{rat}} \equiv \Lambda_1/\Lambda_2$, is approximately equal to q^6 and we test this assumption in Fig. 5. Similar to the results for $\Lambda_{a,YY}$, we find deviations as large as 40% and deviations that differ between the two EOS models. In effect, these assumptions are not independent of the EOS prior distribution. Presuming $\Lambda_{\text{rat}} = q^6$ will tend to overestimate Λ_{rat} .

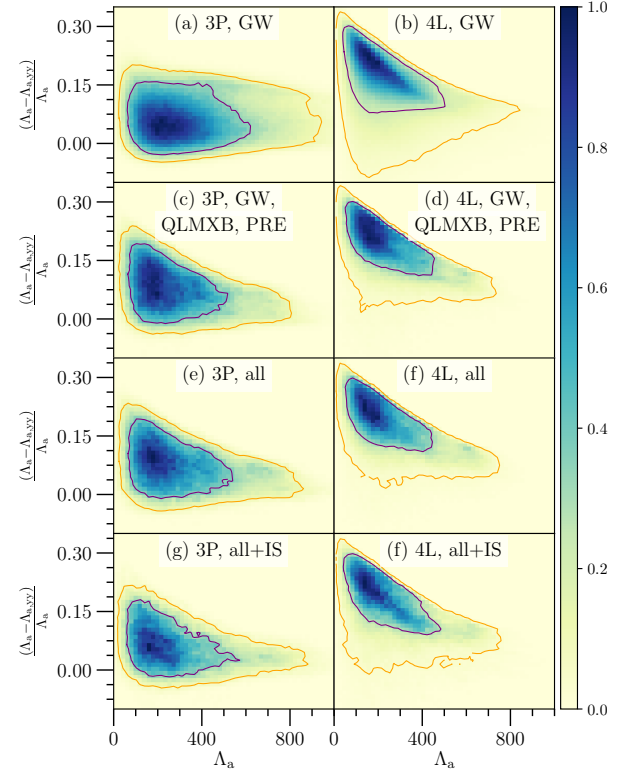


FIG. 4. Joint posterior distribution for the relative deviation between $\Lambda_{a,YY}$ and Λ_a versus Λ_a with contour lines which enclose 68% or 95% of the probability distribution. Panel labeling follows Fig. 1.

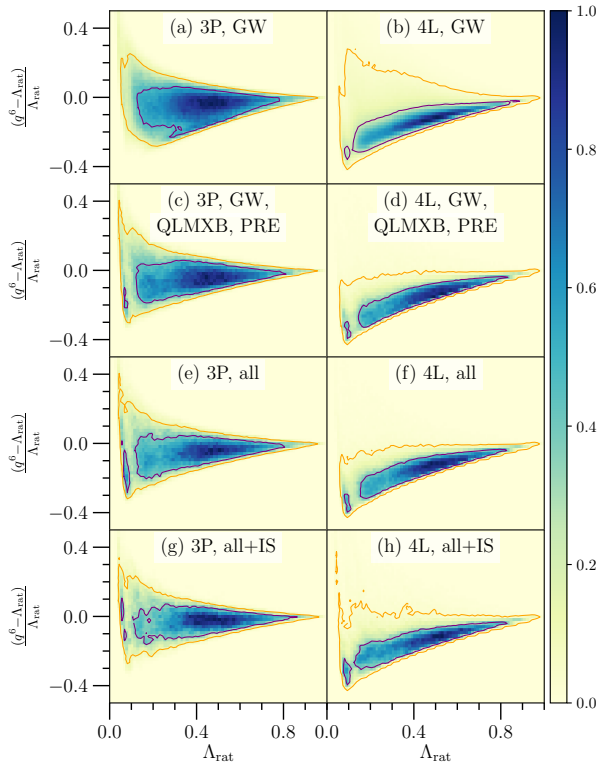


FIG. 5. Joint posterior distribution for the relative deviation between q^6 and Λ_{rat} versus Λ_a with contour lines which enclose 68% or 95% of the probability distribution. Panel labeling follows Fig. 1.

Ref. [34] found a correlation between the compactness and tidal deformability of NS

$$C_i = 3.71 \times 10^{-1} - 3.91 \times 10^{-2} \ln \Lambda_i + 1.056 \times 10^{-3} (\ln \Lambda_i)^2 \quad (11)$$

where $i = \{1, 2\}$ represents the NS in the binary. In Figs. 6 and 7 we compared the compactness (C_{exact}) of the binaries from our posteriors with the relation provided in Eq. (11). We find that this correlation holds for the more massive neutron star to within about 3%, with a peak deviation which depends on the EOS model. For the less massive star, Eq. (11) can be an 8% overestimate; see also an updated analysis on the relationship between C and Λ in Ref. [30].

Radius Correlations

There is a well-known correlation between the symmetry energy slope parameter L and the radius of a 1.4 solar mass neutron star [35], and it has been pointed out previously [29] that this correlation is dependent on the EOS prior distribution. Our joint posteriors are plotted in Fig. 8. The addition of the EM data weakens the correlation, in part simply because of the strong constraint

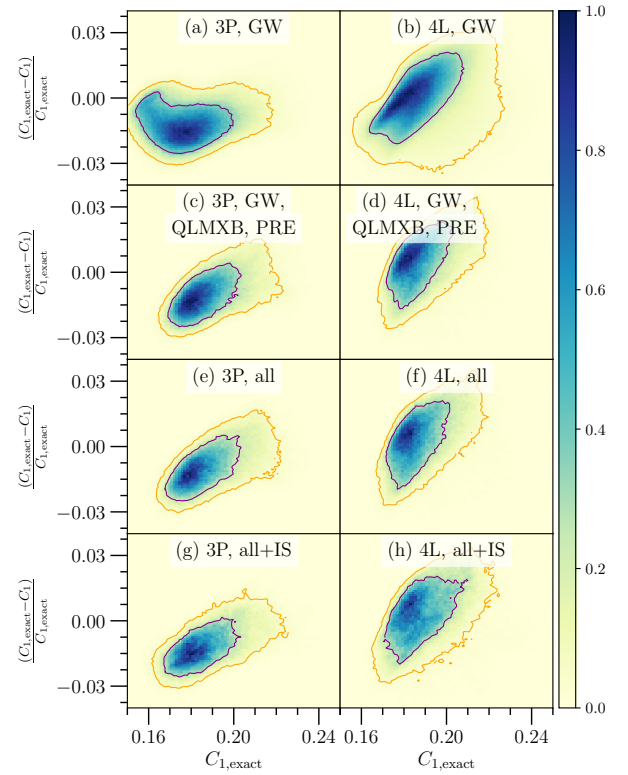


FIG. 6. Joint posterior distribution for the relative deviation between C_1 and $C_{\text{exact},1}$ versus $C_{\text{exact},1}$ with contour lines which enclose 68% or 95% of the probability distribution. Panel labeling follows Fig. 1.

Model	M_{max} vs $R_{1.4}$	L vs $R_{1.4}$
(a) 3P, GW	0.397	0.842
(b) 4L, GW	0.420	0.704
(c) 3P, GW, QLMXB, PRE	0.315	0.558
(d) 4L, GW, QLMXB, PRE	0.167	0.436
(e) 3P, all	0.283	0.575
(f) 4L, all	0.109	0.454
(g) 3P, all+IS	0.381	0.667
(h) 4L, all+IS	0.175	0.496

TABLE VII. Pearson correlation coefficients comparing the radius of a 1.4 solar mass neutron star with the slope of the symmetry energy, L , and the neutron star maximum mass.

on R . A similar correlation has also been suggested between maximum mass of neutron star M_{max} and the corresponding radius [36], but we find this correlation is relatively weak. Pearson correlation coefficients for these two correlations is M_{max} are given in Table VII. The correlations are weaker in the 4L parameterization and the slope of the correlation also depends on the EOS parameterization.

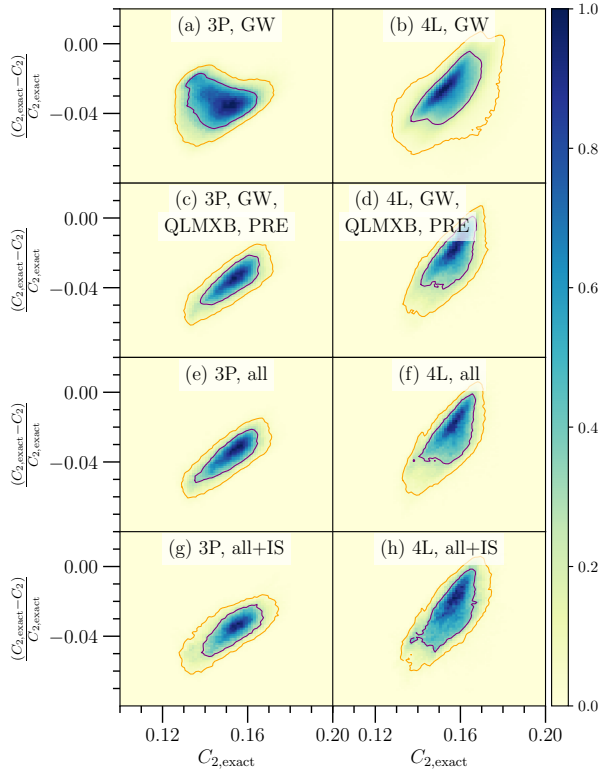


FIG. 7. Joint posterior distribution for the relative deviation between C_2 and $C_{\text{exact},2}$ versus $C_{\text{exact},2}$ with contour lines which enclose 68% or 95% of the probability distribution. Panel labeling follows Fig. 1.

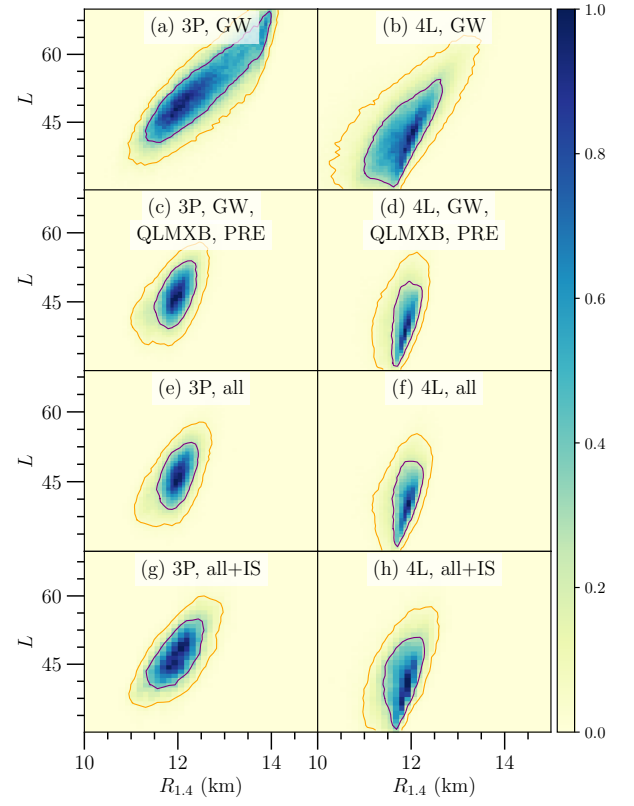


FIG. 8. Distributions for the cross correlation of EOS parameter L with $R_{1.4}$. 3P models have weak correlations of these parameters. But, radius measured in 4L models are nearly independent of EOS parameters.

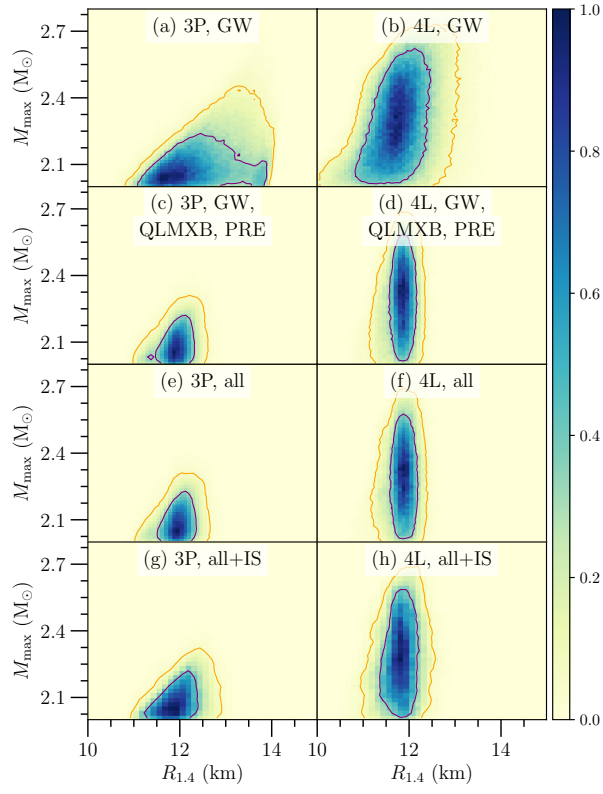


FIG. 9. Plots showing the cross correlation of M_{max} with $R_{1.4}$. 3P and 4L models with the combined analysis of GW and EM data are independent of these parameters.

-
- [1] A. W. Steiner, C. O. Heinke, S. Bogdanov, C. Li, W. C. G. Ho, A. Bahramian, and S. Han, *Mon. Not. R. Astron. Soc.* **476**, 421 (2018), URL <https://doi.org/10.1093/mnras/sty215>.
- [2] A. W. Shaw, C. O. Heinke, A. W. Steiner, S. Campana, H. N. Cohn, W. C. G. Ho, P. M. Lugger, and M. Servillat, *Mon. Not. R. Astron. Soc.* **476**, 4713 (2018), URL <https://doi.org/10.1093/mnras/sty582>.
- [3] J. Nättilä, A. W. Steiner, J. J. E. Kajava, V. F. Suleimanov, and J. Poutanen, *Astron. Astrophys.* **591**, A25 (2016), URL <https://doi.org/10.1051/0004-6361/201527416>.
- [4] J. Nättilä, M. C. Miller, A. W. Steiner, J. J. E. Kajava, V. F. Suleimanov, and J. Poutanen, *Astron. and Astrophys.* **608**, A31 (2017), URL <https://doi.org/10.1051/0004-6361/201731082>.
- [5] J. J. E. Kajava, J. Nättilä, O.-M. Latvala, M. Pursiainen, J. Poutanen, V. F. Suleimanov, M. G. Revnivtsev, E. Kuulkers, and D. K. Galloway, *Mon. Not. R. Astron. Soc.* **445**, 4218 (2014), URL <https://doi.org/10.1093/mnras/stu2073>.
- [6] T. E. Riley, A. L. Watts, S. Bogdanov, P. S. Ray, R. M. Ludlam, S. Guillot, Z. Arzoumanian, C. L. Baker, A. V. Bilous, D. Chakrabarty, et al., *Astrophys. J.* **887**, L21 (2019), URL <https://doi.org/10.3847/2041-8213/ab481c>.
- [7] M. C. Miller et al., *Astrophys. J.* **887**, L24 (2019), URL <https://doi.org/10.3847/2041-8213/ab50c5>.
- [8] LIGO Scientific and Virgo Collaborations, *Phys. Rev. Lett.* **121**, 161101 (2018), URL <https://doi.org/10.1103/PhysRevLett.121.161101>.
- [9] J. Lange, R. O’Shaughnessy, and M. Rizzo, *arXiv:1805.10457* (2018), URL <https://arxiv.org/abs/1805.10457>.
- [10] A. W. Steiner, *arXiv:1802.05339* (2018), URL <https://arxiv.org/abs/1802.05339>.
- [11] S. Gandolfi, J. Lippuner, A. W. Steiner, I. Tews, X. Du, and M. Al-Mamun, *J. Phys. G.* **46**, 103001 (2019), URL <https://doi.org/10.1088/1361-6471/ab29b3>.
- [12] X. Du, A. W. Steiner, and J. W. Holt, *Phys. Rev. C* **99**, 025803 (2019), URL <https://doi.org/10.1103/PhysRevC.99.025803>.
- [13] S. Gandolfi, J. Carlson, and S. Reddy, *Phys. Rev. C* **85**, 032801(R) (2012), URL <https://doi.org/10.1103/PhysRevC.85.032801>.
- [14] J. E. Lynn, I. Tews, J. Carlson, S. Gandolfi, A. Gezerlis, K. E. Schmidt, and A. Schwenk, *Phys. Rev. Lett.* **116**, 062501 (2016), URL <https://doi.org/10.1103/PhysRevLett.116.062501>.
- [15] A. Gezerlis, I. Tews, E. Epelbaum, M. Freunek, S. Gandolfi, K. Hebeler, A. Nogga, and A. Schwenk, *Phys. Rev. C* **90**, 054323 (2014), URL <https://doi.org/10.1103/PhysRevC.90.054323>.
- [16] I. Tews, S. Gandolfi, A. Gezerlis, and A. Schwenk, *Phys. Rev. C* **93**, 024305 (2016), URL <https://doi.org/10.1103/PhysRevC.93.024305>.
- [17] K. E. Schmidt and S. Fantoni, *Phys. Lett. B* **446**, 99 (1999), URL [https://doi.org/10.1016/S0370-2693\(98\)01522-6](https://doi.org/10.1016/S0370-2693(98)01522-6).
- [18] J. D. McDonnell, N. Schunck, D. Higdon, J. Sarich, S. M. Wild, and W. Nazarewicz, *Phys. Rev. Lett.* **114**, 122501 (2015), URL <https://doi.org/10.1103/PhysRevLett.114.122501>.
- [19] M. Kortelainen, J. McDonnell, W. Nazarewicz, E. Olsen, P.-G. Reinhard, J. Sarich, N. Schunck, S. M. Wild, D. Davesne, J. Erler, et al., *Phys. Rev. C* **89**, 054314 (2014), URL <https://doi.org/10.1103/PhysRevC.89.054314>.
- [20] A. W. Steiner, J. M. Lattimer, and E. F. Brown, *Astrophys. J.* **722**, 33 (2010), URL <https://doi.org/10.1088/0004-637X/722/1/33>.
- [21] M. F. Carney, L. E. Wade, and B. S. Irwin, *Phys. Rev. D* **98**, 063004 (2018), URL <https://doi.org/10.1103/PhysRevD.98.063004>.
- [22] R. C. Tolman, *Phys. Rev.* **55**, 364 (1939), URL <https://doi.org/10.1103/PhysRev.55.364>.
- [23] J. Oppenheimer and G. Volkoff, *Phys. Rev.* **55**, 374 (1939), URL <https://doi.org/10.1103/PhysRev.55.374>.
- [24] P. B. Demorest, T. Pennucci, S. M. Ransom, M. S. E. Roberts, and J. W. T. Hessels, *Nature (London)* **467**, 1081 (2010), URL <https://dx.doi.org/10.1038/nature09466>.
- [25] J. Antoniadis, P. C. C. Freire, N. Wex, T. M. Tauris, R. S. Lynch, M. H. van Kerkwijk, M. Kramer, C. Bassa, V. S. Dhillon, T. Driebe, et al., *Science* **340**, 1233232 (2013), URL <https://doi.org/10.1126/science.1233232>.
- [26] H. T. Cromartie, E. Fonseca, S. M. Ransom, P. B. Demorest, Z. Arzoumanian, H. Blumer, P. R. Brook, M. E. DeCesar, T. Dolch, J. A. Ellis, et al., *Nat. Astron.* **4**, 72 (2020), URL <https://doi.org/10.1038/s41550-019-0880-2>.
- [27] J. B. Hartle, *Astrophys. Suppl. Ser.* **24**, 385 (1973), URL <https://doi.org/10.1007/BF02637163>.
- [28] K. Yagi and N. Yunes, *Science* **341**, 365 (2013), URL <https://doi.org/10.1126/science.1236462>.
- [29] A. W. Steiner, J. M. Lattimer, and E. F. Brown, *Eur. Phys. J. A* **52**, 18 (2016), URL <https://doi.org/10.1140/epja/i2016-16018-1>.
- [30] Z. Carson, K. Chatziioannou, C.-J. Haster, K. Yagi, and N. Yunes, *Phys. Rev. D* **99**, 083016 (2019), URL <https://doi.org/10.1103/PhysRevD.99.083016>.
- [31] J. Goodman and J. Weare, *Commun. App. Math. and Comput. Sci.* **5**, 65 (2010), URL <https://doi.org/10.2140/camcos.2010.5.65>.
- [32] K. Yagi and N. Yunes, *Classical and Quantum Gravity* **34**, 015006 (2017), URL <https://doi.org/10.1088/1361-6382/34/1/015006>.
- [33] S. De, D. Finstad, J. M. Lattimer, D. A. Brown, E. Berger, and C. M. Biwer, *Phys. Rev. Lett.* **121**, 091102 (2018), URL <https://doi.org/10.1103/PhysRevLett.121.091102>.
- [34] A. Maselli, V. Cardoso, V. Ferrari, L. Gualtieri, and P. Pani, *Phys. Rev. D* **88**, 023007 (2013), URL <https://doi.org/10.1103/PhysRevD.88.023007>.
- [35] J. M. Lattimer and M. Prakash, *Astrophys. J.* **550**, 426 (2001), URL <https://doi.org/10.1086/319702>.
- [36] C. D. Capano, I. Tews, S. M. Brown, B. Margalit, S. De, S. Kumar, D. A. Brown, B. Krishnan, and S. Reddy, *Nat. Astron.* **4**, 625 (2020), URL <https://doi.org/10.1038/s41550-020-1014-6>.